Postprint of: Nitka M., Tejchman-Konarzewski A., Comparative DEM calculations of fracture process in concrete considering real angular and artificial spherical aggregates, ENGINEERING FRACTURE MECHANICS, Vol. 239 (2020), 107309, DOI: 10.1016/j.engfracmech.2020.107309

Comparative DEM calculations of fracture process in concrete considering real angular and artificial spherical aggregates

M. Nitka and J. Tejchman

Faculty of Civil and Environmental Engineering

Gdańsk University of Technology, Gdańsk, Poland

micnitka@pg.gda.pl, tejchmk@pg.gda.pl

Abstract

Numerical results on a fracture process of a concrete beam with a notch under three-point bending were presented. Calculations were carried out at the concrete aggregate level with the discrete element method (DEM). To explicitly take the heterogeneity into account, concrete was modelled as a four-phase material that included aggregates, cement matrix, interfacial transitional zones (ITZs) and macro-voids. Both the 2D and 3D DEM calculations were performed with the: 1) accurate shape representation of aggregates, based on micro-CT images of concrete and 2) simplified circular/spherical representation of aggregate assuming the same aggregate volume, size and grading curve. In 2D calculations, the positions of circular/spherical aggregate particles were also the same as of real ones. The focus was laid on the impact of the aggregate shape on both the load-displacement curve (strength and brittleness) and fracture geometry (shape, width and length). In addition, the evolutions of broken contacts, contact force networks and tensile stress regions at the crack tip depending upon the aggregate shape were compared with each other. Concrete was proved to be stronger and the macro-crack was less curved for circular/spherical aggregates. Significant dissimilarities regarding the shape of a macro-crack with real aggregates occurred, in particular, for circular/spherical aggregates in 2D simulations.

Keywords: concrete bending; DEM; aggregate shape; strength; fracture

Nomenclature

B	beam width
C	cohesive contact stress
d	particle diameter
E	Young's modulus
E_c	Young's modulus of particle contact
f_c	compressive strength of concrete
$f_{t,flex}$	flexural tensile strength of concrete
F	global vertical force
F^n_{min}	minimum tensile contact force
F^s_{max}	critical cohesive contact force
F_n	normal contact force
F_s	tangential contact force
H	beam height
I	Inertial number
K_n	normal contact stiffness
L	beam length
K_s	tangential contact stiffness
n	number of broken contacts
n'	percent contribution of broken contacts
p	porosity
R_n	normalized roughness
R	particle radius
T	tensile normal contact stress
U	overlap between discrete elements
w	width
v	velocity
α_d	damping parameter
μ	inter-particle friction angle
ν_c	Poisson's ratio of particle contact
ρ	particle mass density

CMOD	crack mouth opening displacement
CT	computed tomography
DEM	discrete element method
FEM	finite element method
ITZ	interfacial transition zone
SEM	scanning electron-microscope
2D	two-dimensional
3D	three-dimensional
‘a’	aggregate
‘cr’	crack
‘cm’	cement matrix
‘damp’	damped
‘max’	maximum
‘min’	minimum

1. Introduction

Concrete is a dominant composite building material in the world in terms of volume that is widely used in the field of civil engineering due to easy fabrication and the lowest ratio between cost and strength as compared to other available materials. It possesses high compressive strength but both low tensile strength and ductility. Thus, it is vulnerable to cracks under static and dynamic loading which are a fundamental phenomenon in concrete materials [1]-[4]. Concrete can be regarded as a homogeneous material at the macro-scale which is a good approximation when designing large structures (the material internal structure is phenomenologically introduced in the constitutive model by some internal length parameters). However, at the mesoscopic level, concrete is a typical composite material consisting of multi-phases, including coarse and fine mineral aggregates, cement matrix, voids and interfacial transition zone (ITZ) between the aggregate and cement matrix. The diameter of coarse aggregates ranges from millimetres to centimetres, whereas ITZs are only several dozen micrometres and the hydrated cement is few nanometres in width. Coarse aggregates with irregular shapes are randomly embedded in the mortar. Porous ITZs are significantly weaker than aggregate and mortar and become attractors for a micro-crack propagation along aggregate boundaries. As a consequence, the concrete structures are

strongly heterogeneous, demonstrating a non-linear stress-strain behaviour [5], [6]. The mesoscopic material heterogeneity has a pronounced influence on complex crack growth trajectory paths at the macro-scale, composed of various macro-crack branches, complementary cracks and micro-cracks [7]-[11]. The mechanical concrete performance depends on material properties of all its constituents and their mutual interaction which makes the modelling of the crack formation and development at the meso-scale a real challenge in terms of efficiency and accuracy. The optimization and safety assessment of structures composed of quasi-brittle materials (like concrete) requires, however, a comprehensive understanding of the behaviour of micro- and macro-cracking and propagation. Recently, great efforts were made to accurately and efficiently capture the failure behaviour of concrete structures at the aggregate level by meso-scale models for a deeper understanding of the mechanisms of damage initiation and fracture evolution. The meso-scale behaviour of concretes may be modelled with continuous (e.g. [12]-[16]) and discontinuous models ([17]-[21]) within continuum mechanics, discrete models, including lattice models (e.g. [22]-[30]), interface models based on fracture mechanics ([31], [32]) and particulate discrete models (e.g. [8], [10], [11], [33]-[39]).

There exist two types of approaches to establish the meso-structure of concrete. The first approach uses the accurate (real) meso-structure of concrete, based on images using the x-ray computed tomography (micro-CT) and scanning electro-microscope (SEM) (e.g. [6]-[8], [13], [34]-[36], [40], [41]). The second simplified approach uses the artificially generated meso-scale model following a specified grading curve using regularly- and non-regularly-shaped aggregate particles (e.g. circles/spheres, ellipses/ellipsoids and polygons/polyhedrons (e.g. [42]-[45])). In most of the numerical mesoscopic studies of concrete, however, the aggregate particles are assumed to be circular in 2D and spherical in 3D conditions to diminish the cost and complexity of model generation. The validity grade of these simplified calculation results provided the motivation to our current numerical investigations.

The main objective of the current paper is two-fold: 1) to clarify the usefulness of circular/spherical aggregate models for studying fracture patterns in concrete under both 2D and 3D conditions and 2) to evaluate and explain the quantitative effect of the shape of aggregate particles on strength, brittleness and fracture in concrete in 2D and 3D conditions with the same material parameters. A notched plain concrete beam under 3-point bending was considered. To address these two significant issues, we performed 2D and 3D comparative

mesoscopic calculations with: 1) real angular aggregate particles, based on micro-CT scans during experiments and 2) artificial circular/spherical aggregate particles which are the novel points in the paper. The latter had the same size, volume and grading curve in 3D conditions (in 2D simulations, their positions were also identical). Such comparative mesoscopic calculations were not performed yet. The simulations were carried out with the discrete element method (DEM). The 3D particulate discrete element model YADE was employed that was developed at the University of Grenoble [46], [47]. DEM allows us for direct simulations of the concrete meso-structure and comprehensive studies of the initiation, growth and formation of cracks which affect the macroscopic concrete behaviour [8], [10], [11], [48]-[51]. DEM demonstrated the ability to account for all failure modes. In our two previous papers [8], [10], we described in detail our experiments and 2D and 3D calculation results with the real angular aggregate by taking micro-CT scans into account. Concrete was depicted in DEM as a phase material including four key constituents: aggregate, cement matrix, interfacial transitional zones (ITZs) and macro-voids. Such 3D comparative calculations concerning the effect of the aggregate shape were already carried out using mesoscopic continuum models (e.g. [7], [21]), but not using DEM that in particular usable for studying the nature of a fracture process at the aggregate level [10], [11]. As compared to mesoscopic continuum calculations, DEM is able to simulate fracture from the beginning of deformation since it possesses strongly diverse local failure criteria. It does not also need softening to be imposed. In addition, the evolution of broken contacts, contact force network and tensile region for the different aggregate shape was compared in 2D and 3D analyses. The DEM calculations are able to replace costly laboratory tests for exploring e.g. the impact of different concrete meso-structures (without and with different additives) on its macroscopic behaviour for receiving its optimum regarding the strength and ductility.

It has been known that the shape of aggregates is of importance for the concrete behaviour. Round aggregates usually display a smooth distribution of stresses at the meso-scale, whereas angular aggregates are associated with local stress concentrations at sharp edges of polygonal particles that can induce micro-cracks. Thus, the tensile strength of concrete with round aggregates becomes higher. On the other hand, round aggregates indicate the lower interlocking action and thus, the concrete with angular aggregates may be stronger. According to mesoscopic FE calculations (e.g. [7], [14], [20], [21], [52]-[55]), the aggregate shape had a certain effect on the ultimate strength of concrete and on the strain to damage-onset and a significant one on the crack initiation, propagation and distribution. The ultimate tensile

strength, strain at the damage onset and brittleness became higher, and the macro-cracks were less curved for circular/spherical grain models. The effect of the aggregate shape on the strength was also closely connected in simulations with the grain size distribution curve [53].

There exist also some experiments, demonstrating the effect of the aggregate shape on the mechanical performance of concrete [56]-[61]. The test results are, however, contradictory. The experimental tensile strength of concrete was found to grow with the angularity [57]-[60], [62] or to reduce [57] or be the same [60]. In [60], concrete made with angular (crushed) aggregates gave the higher elasticity modulus (strong matrix-aggregate interfaces) or lower (weak matrix-aggregate interfaces) than concrete made with oval aggregate particles. The tensile strength showed almost no dependence on the aggregate shape. The fracture energy was higher for angular aggregates. The critical crack opening was either higher (strong matrix–aggregate interfaces) and lower (weak matrix–aggregate interfaces) for spherical aggregates. However, the same aggregate roughness and the related strength and thickness of ITZs (which are very influential mechanical factors) were not preserved in the experiments. Concretes with higher both aggregate roughness, ITZ stiffness and ITZ strength and smaller ITZ thickness produce higher tensile strengths [8], [10], [11], [62],-[64]. For this reason, the experiments on the effect of the aggregate shape on the tensile strength of concrete may result in strongly different results.

The paper is structured as follows. After the introduction (Section 1), our experiments on concrete were very briefly summarized (Section 2). Next, we detailed our numerical approach and input data in Section 3. The effects of the aggregate shape on the load-displacement diagram and crack pattern with crucial findings were discussed in Sections 4 (2D DEM analyses) and 5 (3D DEM analyses). Finally, the summary and conclusions were offered in Section 6.

2. Own experiments on concrete beams

The experimental data of three-point bending concrete beam with a notch were described in detail in our papers [8], [10], [11]. Below, the most important data are reminded. The dimensions of the beams were 320×80×40 mm^3 (length L, height H and width B). The support distance was 240 mm (3×H) (Fig.1). The concrete mixture contained the ordinary

Portland cement, round-shaped gravel and sand particles with the maximum aggregate d_{max}=16 mm and mean aggregate d_{50}=2 mm [8]. The aggregates greater or equal to 2 mm in diameter filled the specimen in 37% [8], [65]. The aggregate surfaces were smooth, i.e. the maximum normalized roughness $R_{n(max)}$, which was expressed as the ratio between the maximum mean distance between the peaks and valleys along the aggregate surface, and the aggregate diameter was low ($R_{n(max)}$=0.045) [11]. The micro-porosity of the mortar was established at the p=5% level in the x-ray micro-CT measurements [65]. The compressive strength of concrete was f_c=51.81 MPa, Young's modulus was E=36.1 GPa, the Poisson's ratio was v=0.22 and the flexural tensile strength was $f_{t,flex}$=4 MPa [13]. The tests were performed with a constant-controlled notch opening displacement (crack mouth opening displacement (CMOD)). The maximum vertical force F_{max} obtained during three-point bending tests was varied between 2.15 and 2.25 kN ($f_{t,flex}$=3.73-3.91 MPa) [8]. The size, shape and positions of the aggregate and macro-voids were found with micro-CT images of the specimen's mid-part (80×50×40 mm^3). The x-ray micro-tomography system SkyScan 1173 was used; the pixel size varied from 3 μm up to 90 μm [65], [66]. The macro-crack above the beam notch was pronouncedly curved in the 3D space; it occurred by bridging the interfacial cracks (micro-damage first initiated in ITZs [8], [10], [11]). The width of porous ITZs on the concrete surface was between 20-50 μm, measured with the scanning electron microscope (SEM) Hitachi TM303 [8]. ITZs were visible around about 90% of the aggregate circumference (in all aggregates (d_a≥2 mm)) due to the creation of water lenses beneath aggregates during concrete mixing. The experimental porosity of ITZs changed between p=25% (directly at the aggregates) down to p=5% (in the cement matrix) [11]. Based on some nano-indentation tests carried out on the mortar close to aggregate, the modulus of elasticity of ITZs was by 35% smaller than the modulus of elasticity of the mortar [11].

3. Discrete element method (DEM) for concrete

DEM has been recognized as an effective tool in the study of frictional-cohesive granular materials, as it allows particles to be modelled individually and forces of various types to be considered. On one hand, DEM is used for comprehensive studies of mechanisms of the initiation, growth and formation of micro- and macro- cracks in concretes since it can accurately characterize their mechanical behaviour and the fracture propagation pattern [8], [10], [11]. On the other hand, DEM may also be applied for analysing different local

phenomena at the aggregate level (e.g. vortex structures and bottlenecks) for early identifying a final macro-crack location [48], [67], [68]. They can be also successfully employed for effectively investigating a mechanical size effect in concrete [51]. The shortcomings of DEM models are long-lasting computations.

The DEM calculations were performed with the three-dimensional spherical explicit discrete element open code YADE [46], [47]. A soft-particle model was used allowing for a small overlap to be formed between two contacted particles. In DEM, translational and rotational motions of all particles are governed by Newton's second law of motion using an explicit time-stepping scheme [69]. Our DEM phase-model for concrete was described in detail in [8], [10], [11]. Its applicability was evaluated by performing a series of simple tests (uniaxial compression, splitting tension, bending). The DEM model faithfully reproduced fracture in concretes under bending (2D and 3D analyses) [8], [10], uniaxial compression (2D and 3D simulations) [48], [49], and splitting tension (2D studies) [50], [51], and shear localization in granular materials [70]-[74]. A cohesive bond was assumed at the particle contact that exhibited the brittle failure under the critical normal tensile load [75]. The tensile failure induced contact separation. The shear cohesion failure initiated contact slip and sliding obeying the Coulomb friction law under normal compression. It can be summarized as follows (Eqs.1-7, Fig.2):

$$\vec{F}_n = K_n U \vec{N}, \tag{1}$$

$$\vec{F}_s = \vec{F}_{s,prev} + K_s \Delta \vec{X}_s, \tag{2}$$

$$K_n = E_c \frac{2R_A R_B}{R_A + R_B} \quad \text{and} \quad K_s = v_c E_c \frac{2R_A R_B}{R_A + R_B}, \tag{3}$$

$$\left\|\vec{F}_s\right\| - F^s_{max} - \left\|\vec{F}_n\right\| \times tan\mu \leq 0 \quad \text{(before contact breakage)}, \tag{4}$$

$$\left\|\vec{F}_s\right\| - \left\|\vec{F}_n\right\| \times tan\mu \leq 0 \quad \text{(after contact breakage)}, \tag{5}$$

$$F^s_{max} = CR^2 \quad \text{and} \quad F^n_{min} = TR^2, \tag{6}$$

$$\vec{F}^k_{damp} = \vec{F}^k - \alpha_d \cdot sgn\left(\vec{v}^k_p\right)\vec{F}^k. \tag{7}$$

where $\vec{F}_n$ - the normal contact force, U - the overlap between discrete elements, $\vec{N}$ - the unit normal vector at each contact point, $\vec{F}_s$ - the tangential contact force, $\vec{F}_{s,prev}$ - the tangential contact force from the previous iteration, $\vec{X}_s$ - the relative tangential displacement increment, K_n - the normal contact stiffness, K_s - the tangential contact stiffness, E_c, - Young's modulus of the particle contact, ν_c - the Poisson's ratio of particle contact, R - the particle radius, R_A and

R_B - the contacting particle radii μ - the Coulomb inter-particle friction angle, F^s_{max} - the critical cohesive contact force, F^n_{min} - the minimum tensile force, C - the cohesive contact stress (maximum shear stress at the pressure equal to zero) and T - the tensile normal contact stress, $\vec{F}^k_{damp}$ - the damped contact force, $\vec{F}^k$ and $\vec{v}^k_p$ - the k^{th} components of the residual force and translational particle velocity v_p and α_d - the positive damping coefficient smaller than 1 (sgn(•) returns the sign of the k^{th} component of velocity). If any contact between spheres after failure re-appeared, the cohesion did not turn up (Eq.5). Note that material softening was not assumed in the DEM model. Albeit bonds could break by shear, the essential micro-scale mechanism for damage in the pre-failure regime was the bond breakage in tension [51]. Five main local material parameters are required for discrete simulations: E_c, υ_c, μ, C and T. The remaining ones are: the particle radii R, particle mass density ρ and damping parameters α_d. The detailed calibration procedure was described in [8], [10], [48], based on simple standard laboratory tests of concrete specimens due to a data lack regarding mechanical properties of ITZs. In the model, the particle breakage was not taken into account. In the calculations with our combined DEM/x-ray μ-CT images mesoscopic approach, ITZs had no physical width and were always simulated by weaker contacts between aggregates and mortar paste. Such an approach was effective enough to capture mechanical fracture [8], [10], [48]-[51]. In [11], the DEM model was improved by extending porous ITZs with a defined thickness around all aggregate particles. However, for 3D analyses, this improved DEM model was very much time-consuming. Therefore, concrete was described in DEM computations as a four-phase material composed of aggregate, cement matrix, ITZs and macro-voids, wherein ITZs had a 0-width. The four-phase material was in the beam mid-region only (Fig.3A). The remaining beam region (outside the meso-region close to the notch) was simulated with the aid of the spheres of d=2-8 mm in order to reduce the calculation time (Fig.3A).

All aggregate particles in the range of 2 mm<d≤16 mm were created as grain clusters with a diameter of d=0.5 mm connected to each other as rigid bodies; they included ITZs. The aggregate volume was as in the experiment (37%). The volume/area, grading curve, shape and position of the aggregate particles were determined by means of micro-CT images [8]. The aggregate particles imbedded in concrete were also modelled as circles/spheres for comparison purposes. In the 2D approach, they preserved either the same area, grading curve and positions (Fig.3Bb) and the same area and grading curve at a random distribution (Fig.3Bc). In the 3D approach, they preserved the same volume and grading curve at a

random distribution (Fig.3Bc). The cement matrix was modelled with spheres only with the diameter 0.25 mm (2D) - 0.35 mm (3D) $\leq d < 2$ mm without ITZs. The cement matrix grains filled in the concrete specimen in p=95% in volume as in the experiment ($p=V_v/V$, V_v - the pore volume and V - the specimen volume). The macro-voids ($d\geq$0.8 mm) were assumed as the empty spaces. In 2D calculations, the width of the beam included one row of aggregate and cement matrix particles along with the beam height. In 3D studies, the beam depth was B=40 mm as in the experiment (Fig.1). The concrete specimens' construction was fully described in [8], [10]. In order to induce the quasi-static deformation in the assembly, the constant velocity of v=2 mm/s was applied at the place of the vertical force F. The prescribed velocity and damping parameter α_d (Eq.7) did not affect the results [48]. The calculated nominal inertial number I (which quantifies the significance of dynamic effects) was $<10^{-3}$ that always corresponded to a quasi-static regime.

The following parameters were used in the beam meso-region in all 2D and 3D calculations [8]: cement matrix (E_{cm}=11.2 GPa, C_{cm}=140 MPa and T_{cm}=22.5 MPa) and ITZs (E_{ITZ}=7.84 GPa, C_{ITZ}=100 MPa and T_{ITZ}=15 MPa). The ratios E_{ITZ}/E_{cm}, C_{ITZ}/C_{cm} and T_{ITZ}/T_{cm} were 0.70. The remaining region with large grains (outside the meso-region) was described by the constants similar as for the mortar [8], [10]. The remaining parameters were constant for all phases and regions: υ_c=0.2 (Poisson's ratio of grain contact), μ=18^o (inter-particle friction angle), α_d=0.08 (damping parameter) and ρ=2600 kg/m^3 (mass density).

The total number of elements was about 25 000 elements (20 000 elements in the meso-region) with the minimum particles diameter d_{min}=0.25 mm in 2D calculations and 235 000 (220 000 in the meso region) with d_{min}=0.35 mm (Fig.3) in 3D calculation. The effect of d_{min} on the stress-strain curve was negligible if d_{min} was small enough, i.e. d_{min}<0.5 mm [48], [49].

4. Two-dimensional simulation results

Strength and brittleness

Figure 4 shows the calculated macroscopic force F versus the CMOD displacement for two types of aggregate from 2D DEM analyses (at the depth of 3 mm from the beam front side) as compared to one experimental curve [8]. The numerical strength of the beams with circular aggregate particles in the beam mid-region was larger by about 15% than with real aggregate

particles, similarly as in other numerical mesoscopic simulations [7], [14], [20], [21], [53]-[55]. The CMOD displacement corresponding to the maximum force was also larger (0.0185-0.019 mm against 0.018 mm). The response of the beam with circular aggregate was more brittle. The best agreement was obviously achieved when the real irregularly-shaped aggregate particles were used. In this case, the maximum calculated vertical force was equal to F=2.20 kN for CMOD=0.018 mm and was almost the same as in the experiment (F=2.18 kN for CMOD=0.017 mm). The residual calculated force (for CMOD=0.10 mm) was about 10% higher than in the laboratory test. The position of spherical aggregates had a minor effect on the force-displacement curve. All 2D numerical curves indicated in the post-peak regime some numerical fluctuations.

Cracking

In Fig.5 the numerical and experimental final crack path (Fig.5a) is shown above the beam notch in the vertical cross-section at the depth of 3 mm from the beam face side for CMOD=0.10 mm. Due to the beam imperfection, the macro-crack was created above the notch and then moved upwards due to bending by bridging the interfacial cracks (Figs.5 and 6). The crack was curved due to the presence of aggregates with ITZs. Many small crack branches formed also along the propagation way. The numerical crack trajectory with the real non-regularly-shaped aggregate in the beam mid-region (Fig.5b) was almost identical as in the experiment (Fig.5a). For round aggregate particles, the propagation way of the main macro-crack was different - it was more vertical (Figs.5c and 5d).

The place, shape and width of the isolated plane macro-crack above the beam notch for CMOD=0.10 mm from 2D DEM simulations **(**at the depth of 3 mm from the beam front side) is shown in Fig.6 for real non-regularly-shaped aggregates and random circular aggregates. The calculated macro-crack height h_c after the test was about h_c=48-50 mm (70% of the specimen height) for the non-regular and circular aggregate (Figs.5b and 6). The crack height was equal to 6 mm (non-circular aggregate) and to 8 mm (circular aggregate) for the maximum vertical force F_{max}. The total crack length l_c for non-regularly-shaped aggregates was about l_c=67 mm, similarly as during the experiment, and was significantly longer than for circularly-shaped aggregates (l_c=55-57 mm, Figs.5c and 5d). Thus, the brittleness of the beam with round aggregates was higher. The crack width w_c almost linearly reduced with the height due to bending. The 2D crack width was similar independently of the aggregate: w_c=0.10 mm

(above the notch) and w_c=0.012-0.015 mm (10 mm below the crack tip) (Fig.6). Those values were similar to the experimental test values using DIC [66].

Broken contacts

Both the number *n* and the percent contribution of broken contacts n' in 2D analyses is demonstrated in Fig.7 (the beam mid-region was solely considered). The initial number of all contacts was about 35'000 and the initial co-ordination number (number of contacts per article) was about 5.7 in both the aggregate types. The evolution shape of broken contacts was similar, independently of the aggregate type (Fig.7A). The breakage rate was smaller when the crack moved through the cement matrix and larger when the crack moved through ITZs around large grains [8]. The grain contacts started to break at the same moment (CMOD=0.005 mm), independently of the aggregate shape, i.e. far before the maximum vertical force F_{max} was reached (CMOD=0.018-0.019 mm). For the peak force F_{max} (CMOD=0.018 mm), the number of broken contacts was higher for real angular aggregates. Later (CMOD>0.03 mm), its number and its damage rate became larger with round aggregates (e.g. by 25-50% for CMOD=0.08 mm). The number of broken contacts reached the same level of about 600 at the end of the test (CMOD=0.1 mm), i.e. 1.65% of all initially existing contacts (Fig.7B).

Contact force network

Figure 8 demonstrates the normal and shear contact force network in the beam mid-region for CMOD=0.10 mm. The red lines in Fig.8A denote the high compressive forces (higher than the average ones) and the blue lines the high tensile forces (lower than the average ones). The remaining forces are marked in green. The line thickness represents the magnitude of contact forces between two particles. The majority of the external vertical force was transmitted via force chains (mainly via the so-called strong contact forces - higher than the average ones). The concrete beams with real non-regularly-shaped aggregate and random circular aggregate showed similar behaviour. Some strong compressive forces existed in the top part of the beam under the vertical force *F* and at the macro-crack. The maximum tensile forces were obviously located above the crack tip. More compressive forces were at the macro-crack for real irregularly-shaped aggregates (Fig.8A). However, their maximum values were similar, about 20 N (tensile force at the crack tip) and 50 N (compressive force under the external vertical force *F*). High tangential forces occurred close to the macro-crack edges due to friction between the aggregates that caused the so-called inter-locking effect [75]-[78].

The maximum tangential contact force close to the macro-crack (connected to the maximum normal contact force) was 5 times higher for non-regularly-shaped aggregates than for rounded aggregates (20 N against 4 N) for CMOD=0.10 mm. For the peak load, both the contact forces were still weakly developed.

5. Three-dimensional simulation results

Two different numerical analyses were performed under 3D conditions: 1) with real non-regularly-shaped aggregate and 2) spherical aggregate randomly distributed (using the same volume, size and grading curve of aggregate). A methodology of the preparation of the specimen meso-structure in 3D based on micro-CT scans was described in detail in [10]. It was not possible to create in 3D simulations spherical aggregates with the same volume and position as the real angular aggregates since the spherical aggregates overlapped each other too strongly in the 3D space.

Strength and brittleness

The force-CMOD curves as compared to the experiment are shown in Fig.9. The spherical aggregates again provided the higher maximum force by 15% (F_{max}=2.46 kN) as compared to the real non-regularly-shaped aggregate as in 2D simulations (Fig.4). The displacement corresponding to the maximum force was also higher. The brittleness was, however, similar for two different aggregate shapes. The computed 3D maximum vertical force (F_{max}=2.14 kN for CMOD=0.0175 mm, Fig.9b) for the real aggregate was very similar to the experiment (F_{max}=2.18 kN for CMOD=0.017 mm) (Fig.9a). The 3D residual vertical force was also close to the experimental one up to CMOD=0.075 mm. The initial concrete stiffness and brittleness were also similar. As compared to 2D calculations (Fig.4), the 3D force-CMOD curve was more realistic in spite of a slight increase of the minimum sphere diameter in the mortar (from 0.25 mm up to 0.35 mm). In addition, fewer force fluctuations occurred in the post-peak regime in 3D due to a higher number of discrete elements. The residual ductility of the 3D beam was slightly lower than this in [10] (Fig.10) due to an improved mapping accuracy of aggregates being in very close contact on x-ray micro-CT images.

Cracking

In Fig.11, the calculated final spatial crack path along the beam width *B* was shown for CMOD=0.10 mm (it can be also seen in Figs.14A and 15). The macro-crack was again more curved in the beam with real irregularly-shaped aggregates (Fig.11a) than in the beam with spherical aggregates (Fig.11b). However, the difference in shape was smaller than in 2D analyses. The crack height was 62 mm (real aggregates) and 60 mm (spherical aggregates). The crack width w_c was slightly smaller for real aggregates (0.07/0.05/0.03 mm) than for spherical aggregates (0.08/0.06/0.04 mm) at 10/20/30 mm above the notch at the distance of 3 mm from the front side (as in 2D calculations). The crack area was equal to 46,5 cm^2 (angular aggregates) or 39.74 cm^2 (spherical aggregates). For the cross-section at the distance of 3 mm from the front side, the macro-crack length was equal to 68 mm (real aggregates) and 64 mm (spherical aggregates) (the difference was smaller than in 2D simulations, Figs.5 and 6). In addition, many micro-cracks occurred around aggregates independently of its shape. The shape of the macro-crack with real aggregates was in satisfactory agreement with the experiment [65] (Fig.12).

Broken contacts

Figure 13 shows the change of the number of broken contacts *n* (Fig.13A) and %-contribution of broken contacts *n'* as compared to the total initial contact amount (Fig.13B) during beam deformation. The initial contact number was 640 000 with the coordination number equal to 7.3 for the real and spherical aggregate. The evolution of broken contacts was similar as in 2D analyses (Fig.7), however, it was smoother. The contact breakage started again far before the force peak, i.e. for CMOD=0.03-0.05 mm (it started slightly earlier with the spherical aggregate). For the peak force F_{max} (CMOD=0.018 mm), the number of broken contacts was smaller in real angular aggregates in contrast to 2D results (Fig.7). Thus, the sharp edges of aggregates do not have to contribute to a lower tensile strength due to stress concentrations. The final %-contact damage was again similar for the real angular and spherical aggregate (1.20%) as in 2D calculations. More than 12 times contacts were broken in 3D than in 2D (7500 versus 600, Figs.7A and 13A). The %-content of broken contacts was, however, lower for the aggregate in 3D than in 2D (1.2% against 1.60%).

Contact force network

The map of (A) normal and (B) tangential contact forces between particles from 3D DEM for CMOD=0.10 mm is shown in Fig.14. It was similar to that in 2D calculations (Fig.8A),

however, more tensile contact forces were concentrated at the crack tip. The maximum compressive forces were under the vertical force and along the macro-crack, the maximum tensile forces were located above the crack tip and the maximum tangential forces (connected directly with the normal contact forces) were at the macro-crack. The maximum compressive/tensile forces on both sides of the macro-crack were found to be higher for the real angular aggregate that for the spherical aggregate (CMOD=0.10 mm): 31.4 N versus 28.2 N and 12.6 N versus 8.6 N (Fig.14A). The mean values were 0.37 N and 0.31 N for compressive and tensile contact forces (real aggregates), and 0.25 N and 0.063 N for spherical aggregates. The maximum and mean tangential forces along the macro-crack were 15.5/0.49 N and 6.84/0.26 N for real and spherical aggregates, respectively (Fig.14B). Thus, very strong interlocking happened (Fig.14B) if the irregularly-shaped aggregates were assumed (similarly as in 2D calculations, Fig.8B). The tensile region at the front of the macro-crack was significantly larger for angular than for round aggregates (Fig.14A).

Figure 15 shows the intensity of tensile normal contact forces in 3D DEM for three different CMOD displacements in a vertical cross-sectional slice at 3 mm from the front beam side (CMOD=0.018 mm (peak load), 0.04 mm and 0.10 mm). The stressed region with broken contacts near the tip of a macro-crack was, in particular, pronounced for irregular aggregates and was not small in comparison to the crack length). In both cases, some strongly stressed and broken contacts also occurred far beyond the main macro-crack.

In summary, the tensile strength of concrete was higher in DEM calculations for circular/spherical aggregates due to the smaller length/area of weak ITZs around round aggregates in the strained/stressed region.

6. Conclusions

A 4-phase meso-scale constitutive model for concrete employing a three-dimensional discrete element model was used in the numerical analyses. ITZs were simulated as porous mortar zones around aggregates with a zero-width by reducing their mechanical properties with respect to the mortar. The model's capability to represent the salient features of concrete in terms of strength, brittleness and fracture was confirmed in DEM calculations with real angular aggregates. Our DEM calculations based on the real micro-structure obtained from

x-ray micro-CT images showed realistic correspondence with experiments (strength, brittleness and fracture). The comparative 2D and 3D analyses were conducted with different aggregate shapes to elucidate their effect on the concrete response during bending with respect to the strength and fracture. Two different aggregate shapes assumed: the real irregularly-shaped based on micro-CT scans and the artificial circular/spherical one. From our numerical analyses with the same material parameters, the following conclusions can be offered:

- Some pronounced differences occurred between the simulation results for angular and round aggregates with respect to the strength and fracture geometry of concrete, in particular in 2D conditions.

- The circular/spherical aggregate shape contributed to the beam strength by 15% (in 2D and 3D analyses) as compared to the real angular aggregate due to a smaller length/area of weak ITZs around round aggregates in the strained region. The calculated concrete brittleness was higher in 2D analyses and similar in 3D ones. The displacement corresponding to the strength was higher for circular/spherical aggregates. The beam strength and brittleness were more realistically reproduced in 3D simulations than in 2D ones.

- The aggregate shape clearly affected the curvature and length of the discrete macro-crack that was created by bridging the interfacial micro-cracks. The crack was more vertical and shorter in length with circular/spherical aggregates, in particular, in 2D analyses. The crack width was slightly higher for spherical aggregates than for real angular aggregates.

- Evident compressive normal and tangential contact forces occurred along the macro-crack due to aggregate inter-locking. They were all significantly stronger for angular aggregates than for spherical ones (by 20-150% in 3D).

- The number of broken normal contacts was higher about 12 times in the 3D beam than in the 2D beam. The final %-contact damage was lower in the 3D beam (1.20%) than in the 2D beam (1.60%).

- The tensile stressed region in the front of the crack tip was larger for irregularly-shaped aggregates.

Acknowledgements

The research work has been carried out within the project "*Effect of meso-structure of concrete on a crack formation and propagation - experiments and two-scale numerical model*" financed by the National Science Centre (NCN) (UMO-2017/25/B/ST8/02108).

References

[1] Carpinteri A., Ingraffea A.R. *Fracture mechanics of concrete* (Martinus Nijhoff, ed.), The Netherlands, 1984.

[2] Bažant Z., Planas J. *Fracture and size effect in concrete and other quasi-brittle materials*, CRC Press LLC, Boca Raton, 1997.

[3] van Mier J.G.M. *Fracture processes of concrete*. CRC press, 2017.

[4] Tejchman J., Bobinski J. *Continuous and discontinuous modelling of fracture in concrete using FEM*. Springer, Berlin-Heidelberg (eds. W. Wu and R. I. Borja), 2013.

[5] Pichler B., Hellmich C. Upscaling quasi-brittle strength of cement paste and mortar: A multi-scale engineering mechanics model. *Cement and Concrete Research* 2011; 41: 467-76.

[6] Königsberger M, Hlobil M, Delsaute B, Staquet S, Hellmich Ch, Pichler B. Hydrate failure in ITZ governs concrete strength: A micro-to-macro validated engineering mechanics model. *Cement and Concrete Research* 2018; 103:77–94.

[7] Du C., Sun L., Jiang S., Ying Z. Numerical simulation of aggregate shapes of three-dimensional concrete and its applications. *Journal of Aerospace Engineering* 2013; 515-527.

[8] Skarżyński L., Nitka M., Tejchman J. Modelling of concrete fracture at aggregate level using FEM and DEM based on x-ray μCT images of internal structure. *Engineering Fracture Mechanics* 2015; 10 (147): 13-35.

[9] Ren W., Yang Z., Sharma R., Zhang C., Withers P.J. Two-dimensional X-ray CT image based meso-scale fracture modelling of concrete. *Engineering Fracture Mechanics* 2015; 133, 24-39.

[10] Nitka M., Tejchman J. A three-dimensional meso scale approach to concrete fracture based on combined DEM with X-ray μCT images. *Cement and Concrete Research* 2018; 107, 11-29.

[11] Nitka M., Tejchman J. Meso-mechanical modelling of damage in concrete using discrete element method with porous ITZs of defined width around aggregates. *Engineering Fracture Mechanics* 2020; 231, 107029.

[12] Gitman I.M., Askes H., Sluys L.J. Coupled-volume multi-scale modelling of quasi-brittle material. *European Journal of Mechanics A/Solids* 2008; 27:302-327

[13] Skarżyński Ł, Tejchman J. Calculations of fracture process zones on meso-scale in notched concrete beams subjected to three-point bending. *European Journal of Mechanics* A/Solids 2010; 29 (4):746-760

[14] Kim S.M., Abu Al-Rub R.K. Meso-scale computational modeling of the plastic-damage response of cementitious composites. *Cement and Concrete Research* 2011; 41:339-358.

[15] Shahbeyk S., Hosseini M., Yaghoobi M. Mesoscale finite element prediction of concrete failure. *Computational Materials Science* 2011; 50 (7):1973-1990.

[16] Zhou R., Chen H.-H. Mesoscopic investigation of size effect in fracture process zone. *Engineering Fracture Mechanics* 2019; 212, 136-152.

[17] Yang Z.J. Su, X.T. Chen J.F. Liu G.H. Monte Carlo simulation of complex cohesive fracture in random heterogeneous quasi-brittle materials. *Int. J. Solids Struct*. 2009; 46, 3222–3234.

[18] Su X.T. Yang Z.J., Liu G.H. Monte Carlo simulation of complex cohesive fracture in random heterogeneous quasi-brittle materials: A 3D study. *Int. J. Solids Struct*. 2010, 47, 2336–2345.

[19] Wang X.; Zhang M. Jivkov A.P. Computational technology for analysis of 3D meso-structure effects on damage and failure of concrete. *Int. J. Solids Struct*. 2016; 80, 310–333

[20] Trawinski W., Bobinski J., Tejchman J. Two-dimensional simulations of concrete fracture at aggregate level with cohesive elements based on X-ray micro-CT images. *Engineering Fracture Mechanics* 2016; 168, 201-226.

[21] Trawiński W., Tejchman J., Bobiński J. A three-dimensional meso-scale approach with cohesive elements to concrete fracture based on X-ray μCT images. *Engineering Fracture Mechanics* 2018; 189, 27-50.

[22] Herrmann H.J., Hansen A., Roux S. Fracture of disordered, elastic lattices in two dimensions. *Physical Rev B* 1989; 39:637-647

[23] Lilliu G., van Mier J.G.M. 3D lattice type fracture model for concrete. *Engineering Fracture Mechanics* 2003; 70, 927-941.

[24] Schlangen E., Garboczi E.J. New method for simulating fracture using an elastically uniform random geometry lattice. *Internat. J. Engrg. Sci*. 1996; 34, 1131–1144

[25] Kozicki J., Tejchman J. Modelling of fracture processes in concrete using a novel lattice model. *Granular Matter* 2008; 10:377-388

[26] Kozicki J., Tejchman J. Effect of aggregate structure on fracture process in concrete using 2D lattice model. *Archives of Mechanics* 2007; 59, 4-5, 1-20.

[27] Cusatis G., Pelessone D., Mencarelli A. Lattice discrete particle model (LDPM) for failure behavior of concrete. I: theory. *Cem. Concr. Compos*. 2011; 33, 881–890.

[28] Pan Z., Ma R., Wang D., Chen A. A review of lattice type model in fracture mechanics: theory, applications, and perspectives. *Engineering Fracture Mechanics,* 2018; 190:382–409.

[29] Karavelić E., Nikolić M., Ibrahimbegovic A., Kurtović A. Concrete meso-scale model with full set of 3D failure modes with random distribution of aggregate and cement phase. Part I: Formulation and numerical implementation. *Comput. Methods Appl. Mech. Eng.* 2019; 344:1051-1072.

[30] Šavija B., Smith G.E., Liub D., Schlangen E., Flewitt P.E.J. Modelling of deformation and fracture for a model quasi-brittle material with controlled porosity: Synthetic versus real microstructure. *Engineering Fracture Mechanics* 2019; 205, 399-417.

[31] Carol I, López C.M., Roa O. Micromechanical analysis of quasi-brittle materials using fracture-based interface elements. *International Journal for Numerical Methods in Engineering* 2001; 52:193-215

[32] López C.M., Carol I., Aguado, A. Meso-structural study of concrete fracture using interface elements. I: Numerical model and tensile behavior. *Mater. Struct*. 2008; 41, 583–599.

[33] Donze F.V., Magnier S.A., Daudeville L., Mariotti C. Numerical study of compressive behaviour of concrete at high strain rates. *Journal for Engineering Mechanics* 1999; 122(80):1154-1163

[34] Hentz S., Daudeville L., Donze F. Identification and validation of a Discrete Element Model for concrete. *Journal of Engineering Mechanics* ASCE 2004; 130 (6):709-719

[35] Dupray. F, Malecot Y., Daudeville L., Buzaud E.A. Mesoscopic model for the behaviour of concrete under high confinement. *International Journal for Numerical and Analytical Methods in Geomechanics* 2009; 33:1407-23

[36] Groh U., Konietzky H., Walter K. et al. Damage simulation of brittle heterogeneous materials at the grain size level, *Theoretical and Applied Fracture Mechanics* 2011; 55, 31-38.

[37] Rangari S., Murali K., Deb A. Effect of meso-structure on strength and size effect in concrete under compression. *Eng. Fract. Mech*. 2018; 195, 162–185.

[38] Nguyen T.T., Bui H.H., Ngo T.D., Nguyen G.D., Kreher M.U., Darve F. A micromechanical investigation for the effects of pore size and its distribution on geopolymer foam concrete under uniaxial compression. *Eng. Fract. Mech.* 2019; 209, 228–244.

[39] Krenzer K., V. Mechtcherine V., Palzer U. Simulating mixing processes of fresh concrete using the discrete element method (DEM) under consideration of water addition and changes in moisture distribution. *Cement and Concrete Research* 2019; 115, 274–282

[40] Huang Y., Zhenjun Y., Wenyuan R., Liu G., Zhang C. 3D meso-scale fracture modelling and validation of concrete based on in-situ X-ray Computed Tomography images using damage plasticity model. *Int. J. Solids Struct*. 2015; 67-68, 340–352.

[41] Yang Z., Ren W., Sharma R., McDonald S., Mostafavi M., Vertyagina Y., Marrow T.J. In-situ X-ray computed tomography characterisation of 3D fracture evolution and image-based numerical homogenisation of concrete. *Cem. Concr. Compos*. 2017;75:74–83.

[42] Snozzi L., Caballero A., Molinari J.F. Influence of the meso-structure in dynamic fracture simulation of concrete under tensile loading. *Cem. Concr. Res*. 2011; 41, 1130–1142.

[43] Li G., Yu J., Cao P., Ren Z. Experimental and numerical investigation on I–II mixed-mode fracture of concrete based on the Monte Carlo random aggregate distribution. *Constr. Build. Mater*. 2018; 191, 523–534.

[44] Saksala T. Numerical modelling of concrete fracture processes under dynamic loading: Meso-mechanical approach based on embedded discontinuity finite elements. *Eng. Fract. Mech*. 2018; 201, 282–297

[45] Leite J., Slowik V., Mihashi H. Computer simulation of fracture processes of concrete using mesolevel models of lattice structures, *Cem. Concr. Res*. 2004; 34 (6) 1025–1033.

[46] Kozicki J., Donze F. A new open-source software developer for numerical simulations using discrete modeling methods. *Computer Methods in Applied Mechanics and Engineering* 2008; 197:4429-4443.

[47] Šmilauer V., Chareyre B. Yade DEM Formulation. Manual, 2011.

[48] Nitka M., Tejchman J. Modelling of concrete behaviour in uniaxial compression and tension with DEM. *Granular Matter* 2015; 17 (1):145-164

[49] Suchorzewski J., Tejchman J., Nitka M. Discrete element method simulations of fracture in concrete under uniaxial compression based on its real internal structure. *International Journal of Damage Mechanics* 2018; 27(4):578-607.

[50] Suchorzewski J., Tejchman J., Nitka M. Experimental and numerical investigations of concrete behaviour at meso-level during quasi-static splitting tension. *Theoretical and Applied Fracture Mechanics* 2018; 96:720-739.

[51] Suchorzewski J., Tejchman J., Nitka M., Bobiński J. Meso-scale analyses of size effect in brittle materials using DEM. *Granular Matter* 2019; 21 (9):1-19.

[52] He H., Guo Z., Stroeven P., Stroeven M., Sluys L.J. Influence of particle packing on elastic properties of concrete. *Proc First International Conference on Computational Technologies in Concrete Structures* (CTCS'09):1177-1197, 2009.

[53] Skarżyński Ł., Tejchman J. Experimental investigations of fracture process in plain and reinforced concrete beams under bending. *Strain* 2013; 49:521-43.

[54] Skarżyński Ł., Tejchman J. Modelling the effect of composition on the tensile properties of concrete. Understanding the tensile properties of concrete (edited by Jaap Weerheijm). Woodhead Publishing Limited:52-97, 2013.

[55] Zhou Y., Jin H., Wang B. Modeling and mechanical influence of meso-scale concrete considering actual aggregate shapes. *Construction and Building Materials* 2019; 228, 116785

[56] Saouma V.E., Broz J.J., Brühwiler E., Boggs H.L. Effect of aggregate and specimen size on fracture properties of dam concrete. *J Mater Civil Engng* 1991; 3:204–18.

[57] Giaccio G., Zerbino R. Failure mechanism of concrete: combined effects of coarse aggregates and strength level, *Adv. Cem. Based Mater*. 1998; 7, 41–48.

[58] Guinea G.V., El-Sayed K.M., Rocco C., Elices M., Planas J. The effect of the bond between the matrix and the aggregates on the cracking mechanism and fracture parameters of concrete. *Cement Concrete Res* 2002; 32:1961–70.

[59] Li Q., Deng Z., Fu H. Effect of aggregate type on mechanical behaviour of dam concrete. *ACI Mater J* 2004; 101(6):483–92

[60] Rocco C.G., M. Elices M. Effect of aggregate shape on the mechanical properties of a simple concrete. *Engineering Fracture Mechanics* 2009; 76, 286–298

[61] Seung Jae Lee, Chang Hoon Lee, Moochul Shin, Sumana Bhattacharya, Yu Feng Su. Influence of coarse aggregate angularity on the mechanical performance of cement-based materials. *Construction and Building Materials* 2019; 204, 184-19.

[62] Rao G.A., Prasad B.K.R. Influence of type of aggregate and surface roughness on the interface fracture properties, *Mater Struct* 2004; 37(5): 328–333.

[63] Gu X.L., Hong L., Wang Z.L., Lin F. Experimental study and application of mechanical properties for the interface between cobblestone aggregate and mortar in concrete. *Constr Build Mate*r 2013; 46: 156–66.

[64] Hong L., Gu X., Lin F. Influence of aggregate surface roughness on mechanical properties of interface and concrete. *Construction and Building Materials* 2014; 65: 338-349.

[65] Skarżyński Ł., Tejchman J. Experimental investigations of fracture process in concrete by means of x-ray micro-computed tomography. *Strain* 2016; 52, 26-45.

[66] Skarżyński L., Tejchman J. Experimental investigations of damage evolution in concrete during bending by continuous micro-CT scanning. *Materials Characterization* 2019; 154: 40-52.

[67] Tordesillas A., Kahagalage S., Ras C., Nitka M., Tejchman J. Coupled evolution of preferential paths for force and damage in the pre-failure regime in disordered and heterogeneous, quasi-brittle granular materials. *Materials. Front. Mater*. 7:79. doi: 10.3389/fmats.2020.00079, 2020.

[68] Tordesillas A., Kahagalage S., Ras C., Nitka M., Tejchman J. Early prediction of macrocrack location in concrete and other granular composite materials. *Scientific Reports - Energy* 2020 (in review).

[69] Cundall P.A., Strack O.D.L. A discrete numerical model for granular assemblies, *Geotechnique* 1979: 29:47-65.

[70] Kozicki J., Tejchman J., Mróz Z. Effect of grain roughness on strength, volume changes, elastic and dissipated energies during quasi-static homogeneous triaxial compression using DEM. *Granular Matter* 2012; 14:457-68.

[71] Kozicki J., Niedostatkiewicz M., Tejchman J., Mühlhaus H-B, Discrete modelling results of a direct shear test for granular materials versus FE results. *Granular Matter* 2013; 15(5): 607-627.

[72] Kozicki J., Tejchman J., Műhlhaus H.-B. Discrete simulations of a triaxial compression test for sand by DEM, *Int. J. Num. Anal. Methods Geom.* 2014; 38, 1923-1952.

[73] Nitka M., Tejchman J., Kozicki J., Leśniewska D. DEM analysis of micro-structural events within granular shear zones under passive earth pressure conditions. *Granular Matter* 2015; 17(3):325-343.

[74] Kozicki J., Tejchman J. Relationship between vortex structures and shear localization in 3D granular specimens based on combined DEM and Helmholtz-Hodge decomposition. *Granular Matter* 2018; 20(48):1-24.

[75] Ergenzinger C., Seifried R., Eberhard P.A. Discrete Element Model to Describe Failure of Strong Rock in Uniaxial Compression. *Granular Matter* 2011; 13, 4:341-364.

[76] Walraven J.C. Fundamental analysis of aggregate interlock, *J. Struct. Div*. 1981; 107(11): 2245-2270.

[77] Eliâš J., Stang H. Lattice modeling of aggregate interlocking in concrete. *Int. J. Fracture* 2012; 175: 1-11

[78] Scholtès L., Donzé F.V. A DEM model for soft and hard rocks: Role of grain interlocking on strength. *Journal of the Mechanics and Physics of Solids*. 2013; 61(2): 352-369.

LIST OF FIGURES

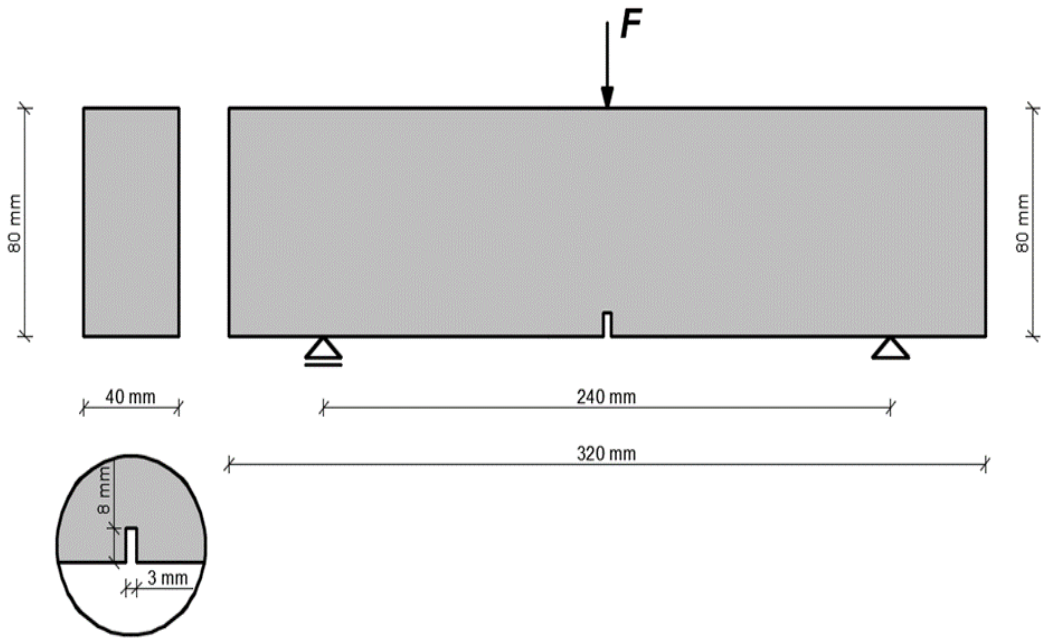

Fig.1: Experiments with concrete under bending: geometry and boundary conditions of concrete beams subjected to three-point bending [8], [10], [65]

FIGURE 1

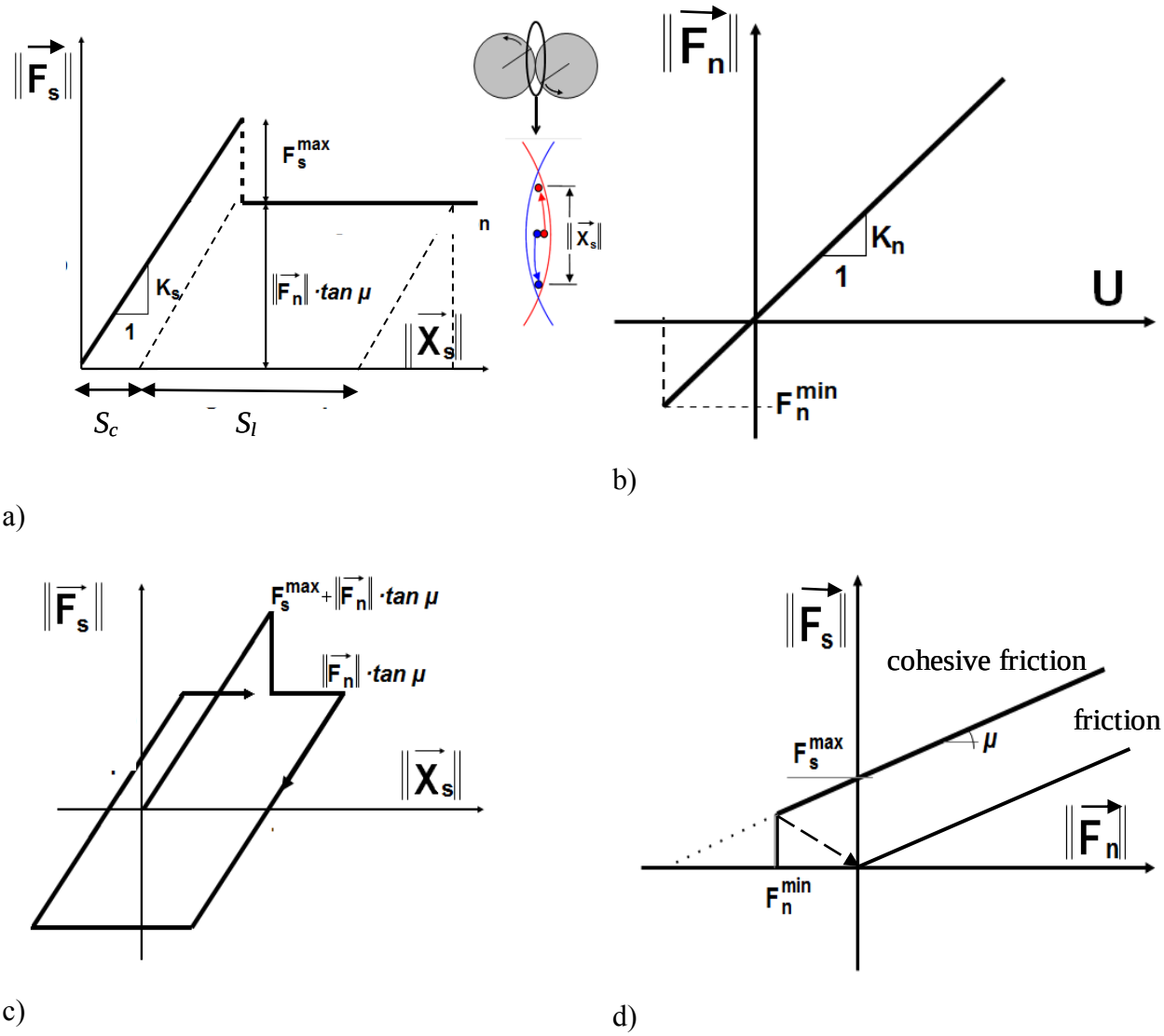

Fig.2: Mechanical response of DEM: a) tangential contact model, b) normal contact model, c) loading and unloading path in tangential contact model and d) modified Mohr-Coulomb model [46], [47]

FIGURE 2

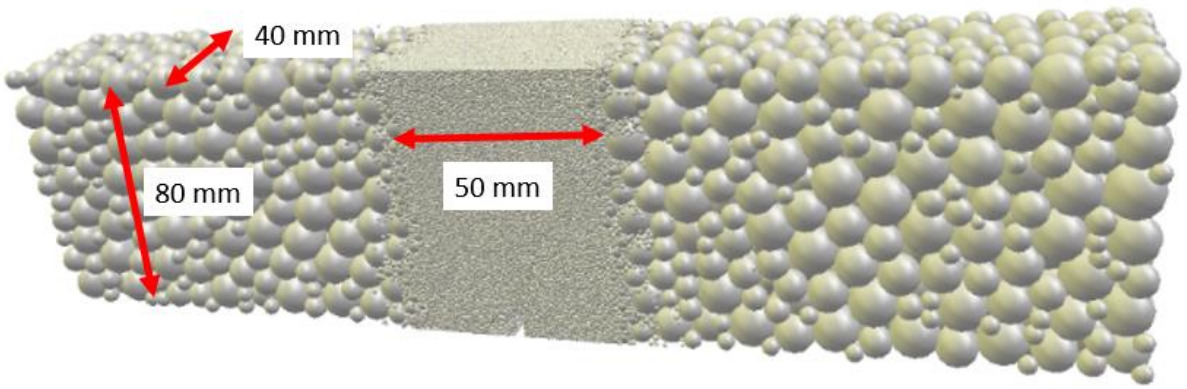

A)

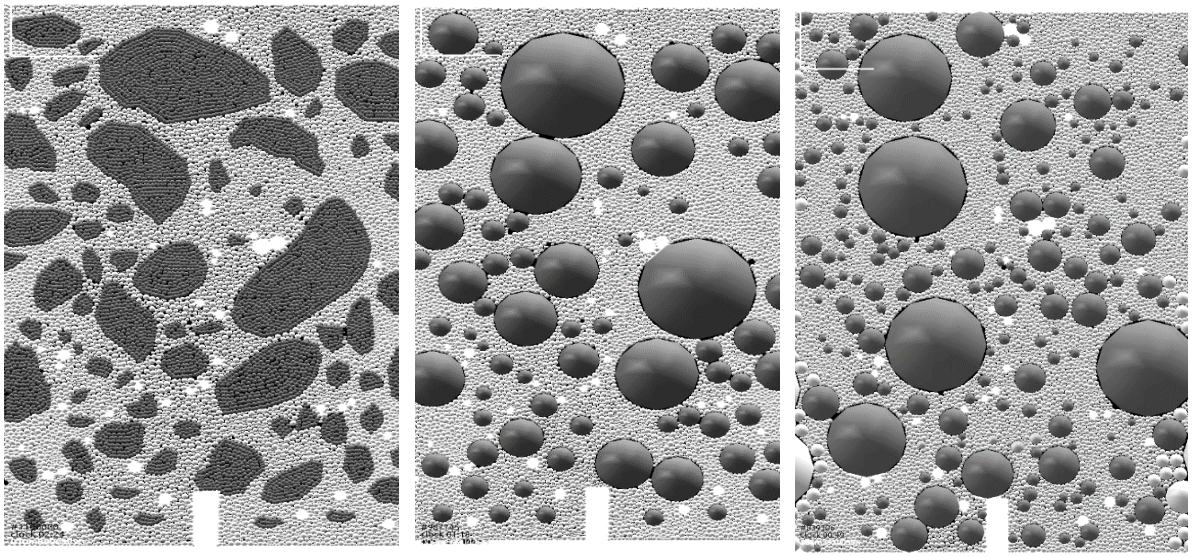

2D

a) b) c)

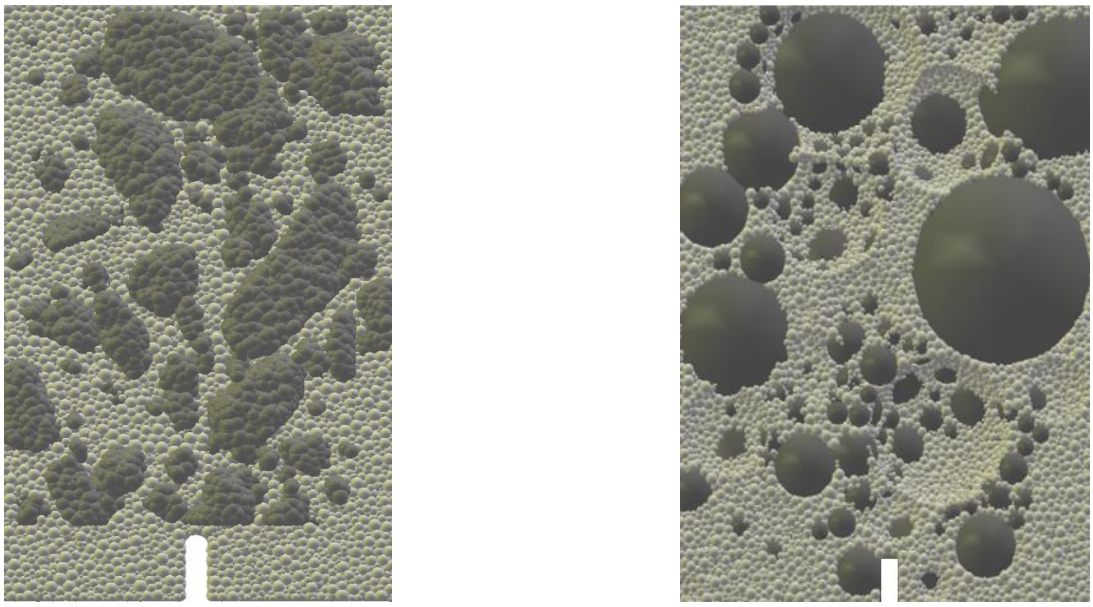

3D

a) c)

B)

Fig.3: 2D and 3D geometry of concrete with different aggregate particles: A) entire 3D beam and B) beam meso-region of 50×80 mm^3 close to notch based on micro-CT images (at 3 mm from specimen front) with aggregates modelled as: a) real non-regularly-shaped aggregates [8], [10]), b) circular aggregates with equivalent cross-sectional area and position and c) randomly distributed circular aggregates with equivalent cross-sectional area (dark grey colour corresponds to aggregate, light grey colour to cement matrix and white spots to macro-voids)

FIGURE 3

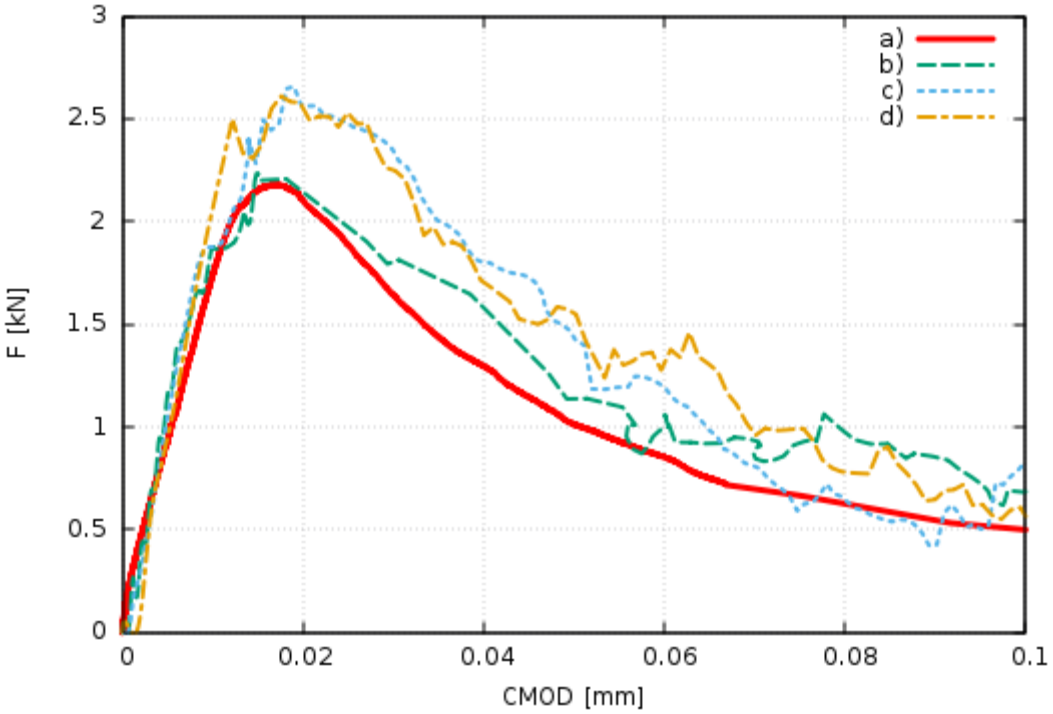

Fig.4: Evolution of vertical force *F* against CMOD displacement in beam under 3-point bending in 2D numerical analyses **(**at depth of 3 mm from beam front side): a) experimental curve [8], b) DEM with real non-regularly-shaped aggregate [8], c) DEM with circular aggregate at same position as in 'b') and d) DEM with circular aggregate at random position

FIGURE 4

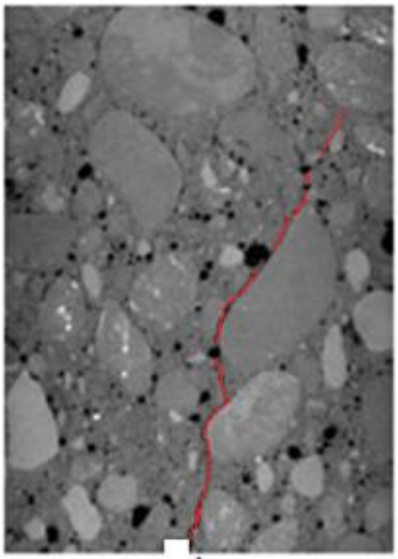

a)

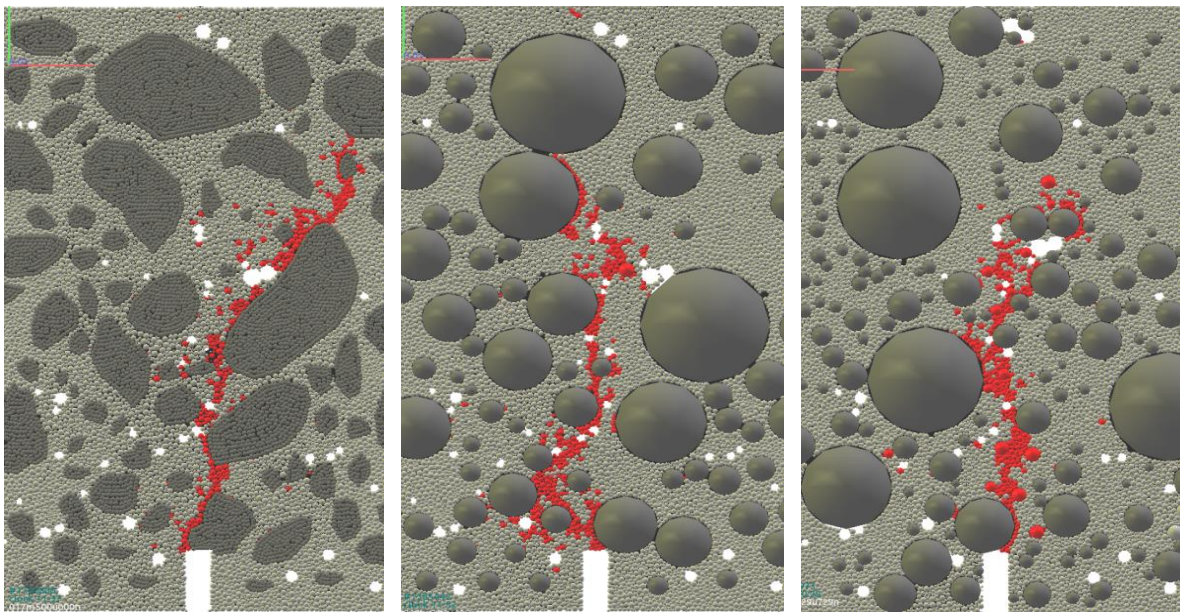

b) c) d)

Fig.5: Final crack trajectory in concrete beam above notch after test for CMOD=0.10 mm: a) µCT-image at depth of 3 mm from beam face side (black colour denotes macro-voids) and b) 2D DEM with real non-regularly-shaped aggregates [8], c) 2D DEM with rounded aggregates at same position and d) 2D DEM with random rounded aggregates (red colour denotes elements with broken contacts, dark grey denotes aggregate, light grey denotes cement matrix and white colour denotes macro-voids)

FIGURE 5

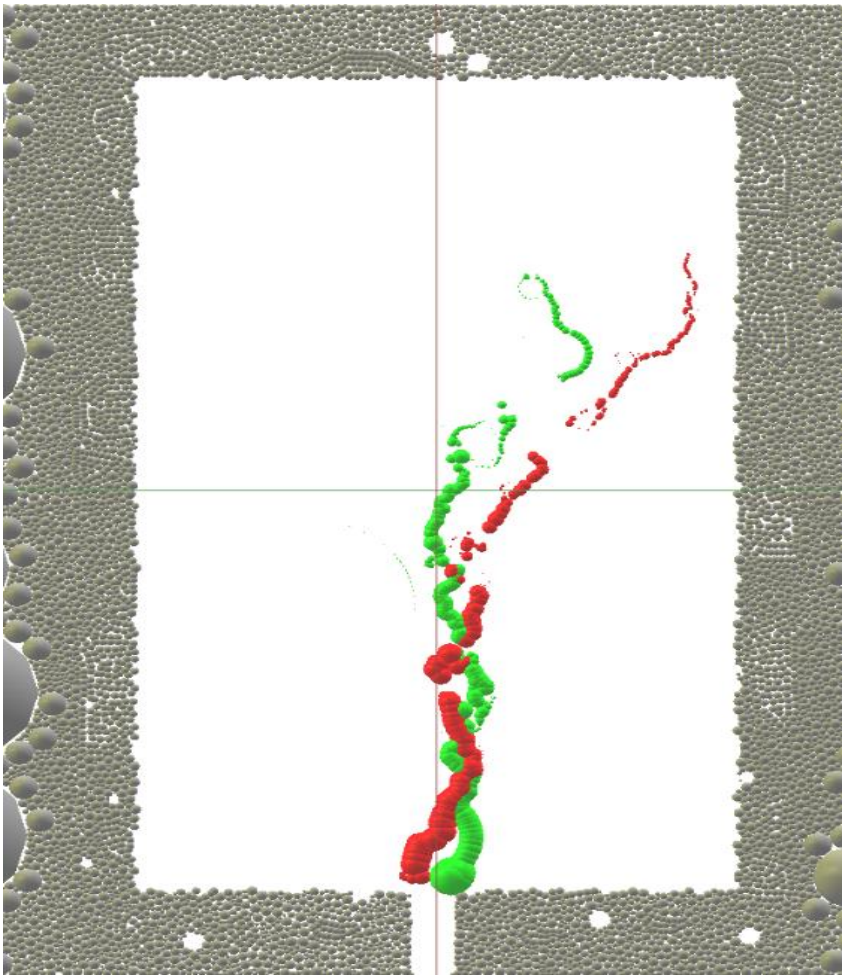

Fig.6: Place, shape and width of isolated plane macro-crack above beam notch for CMOD=0.10 mm from 2D DEM simulations **(**at depth of 3 mm from beam front side): real non-regularly-shaped aggregate (in red) and random circular aggregate (in green) (crack width is multiplied by factor 10, crack width at notch is equal to CMOD)

FIGURE 6

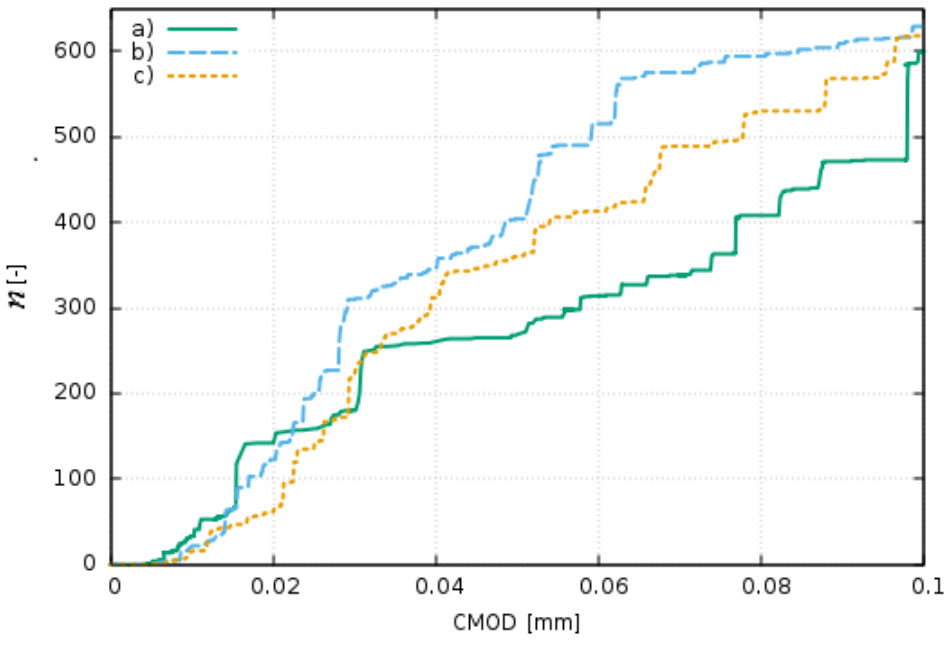

A)

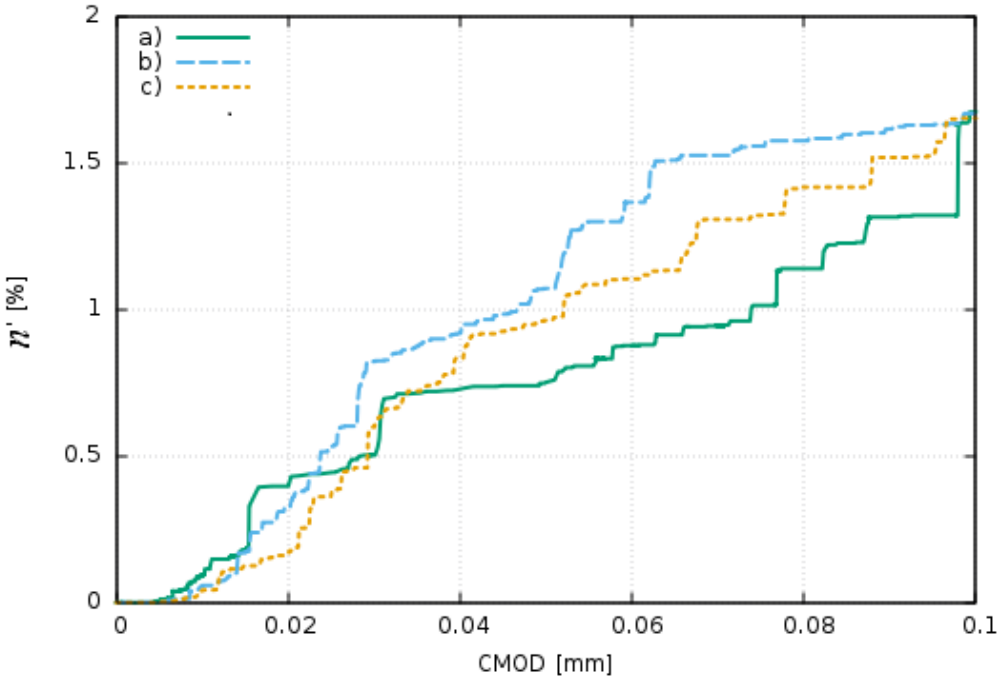

B)

Fig.7: Number of broken contacts *n* (A) and percent content of broken contacts related to initial number of contacts *n'* (B) versus CMOD displacement using 2D DEM with: a) real non-regularly-shaped aggregate [8], b) circular aggregate at same position as in 'a') and c) randomly located circular aggregate

FIGURE 7

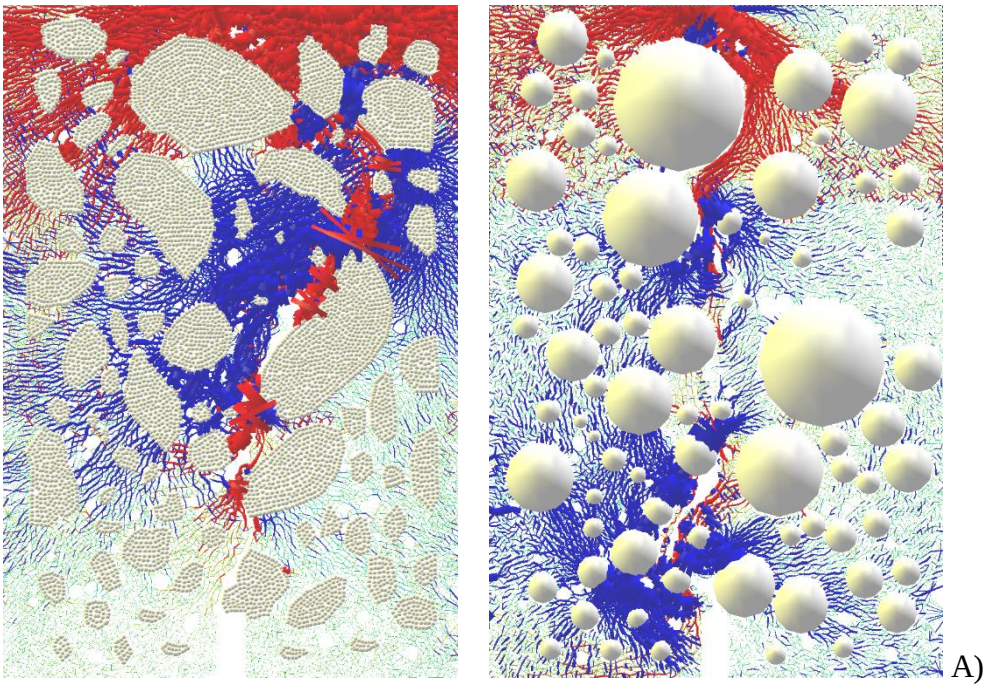

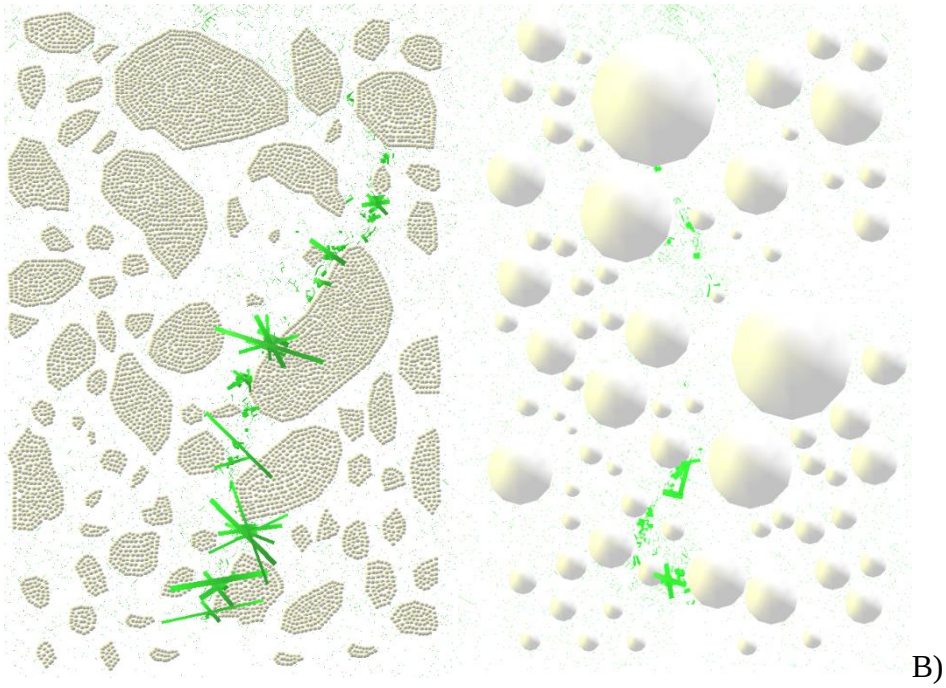

Fig.8: Map of normal (A) and tangential contact forces (B) between particles obtained from 2D DEM for CMOD=0.10 mm with: a) real non-regularly-shaped aggregate [8] and b) randomly distributed circular aggregate (red colour denotes large compressive forces and blue colour denotes large tensile forces, line thickness corresponds to force magnitude)

FIGURE 8

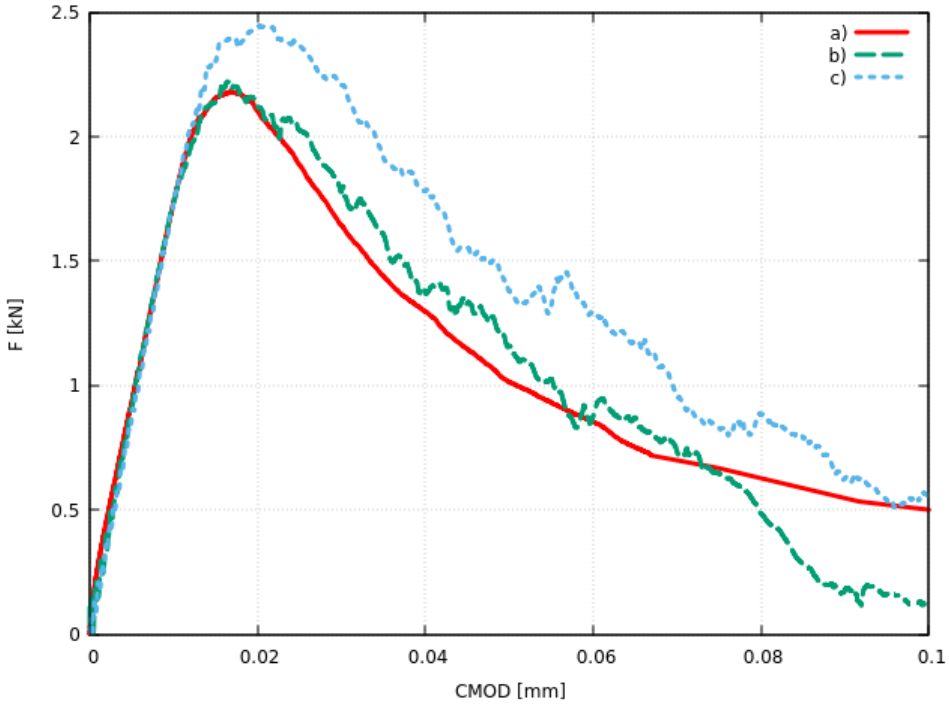

Fig.9: Evolution of vertical force *F* against displacement CMOD in beam under 3-point bending from 3D numerical analyses: a) experimental curve (in red), b) DEM with real irregularly-shaped aggregate (in green) and c) DEM with random spherical aggregate (in blue)

FIGURE 9

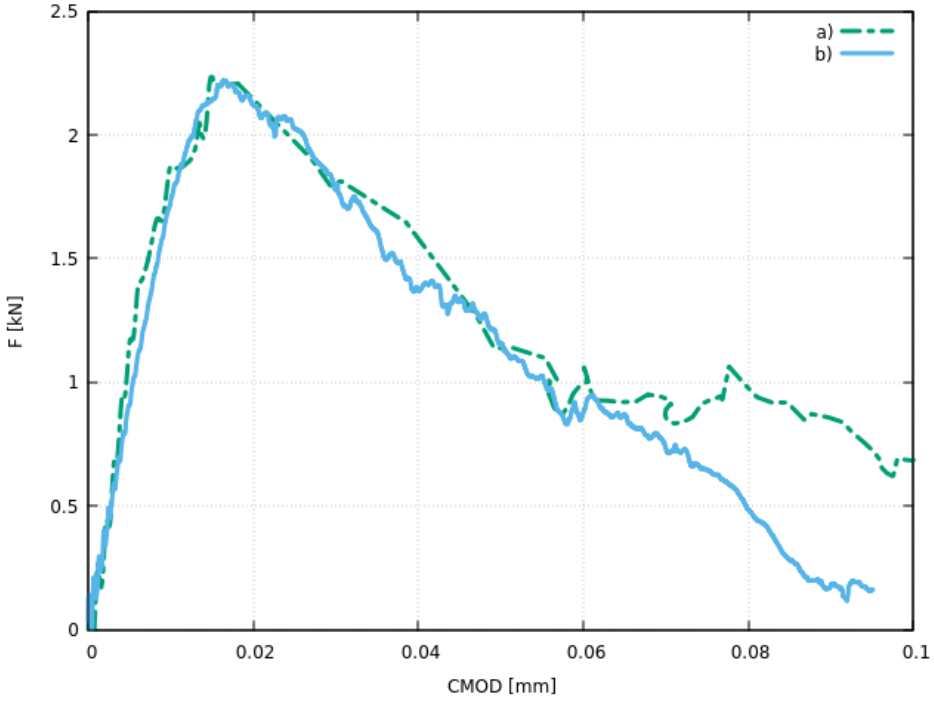

Fig.10: Evolution of vertical force *F* against CMOD in beam under 3-point bending: a) calculated curves [10] (in green) and b) calculated curve (Fig.9b) (in blue)

FIGURE 10

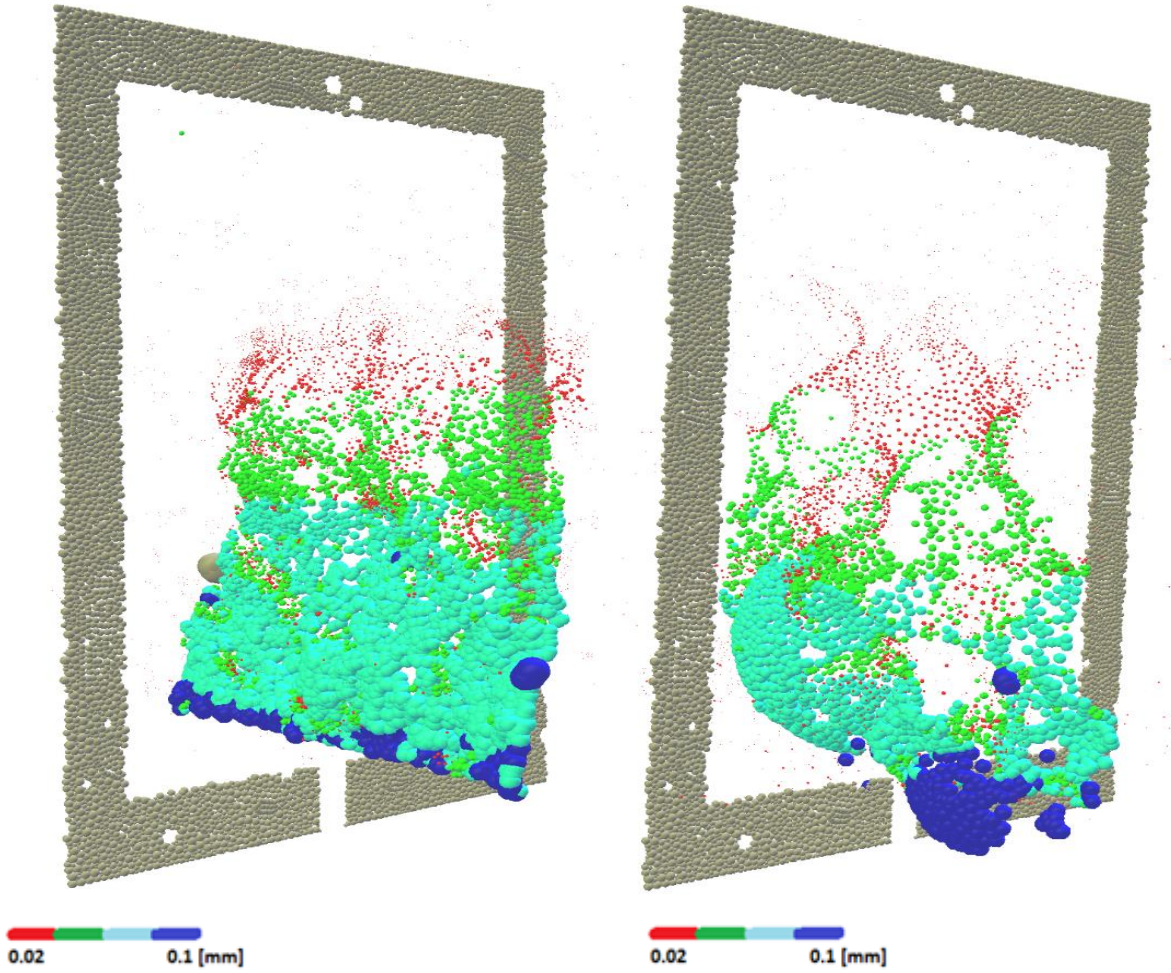

a) b)

Fig.11: Place, shape and width (with scale) of isolated spatial macro-crack above beam notch for CMOD displacement of 0.10 mm from 3D DEM analyses: a) real irregularly-shaped aggregates and b) randomly distributed spherical aggregates (crack width is multiplied by factor 10)

FIGURE 11

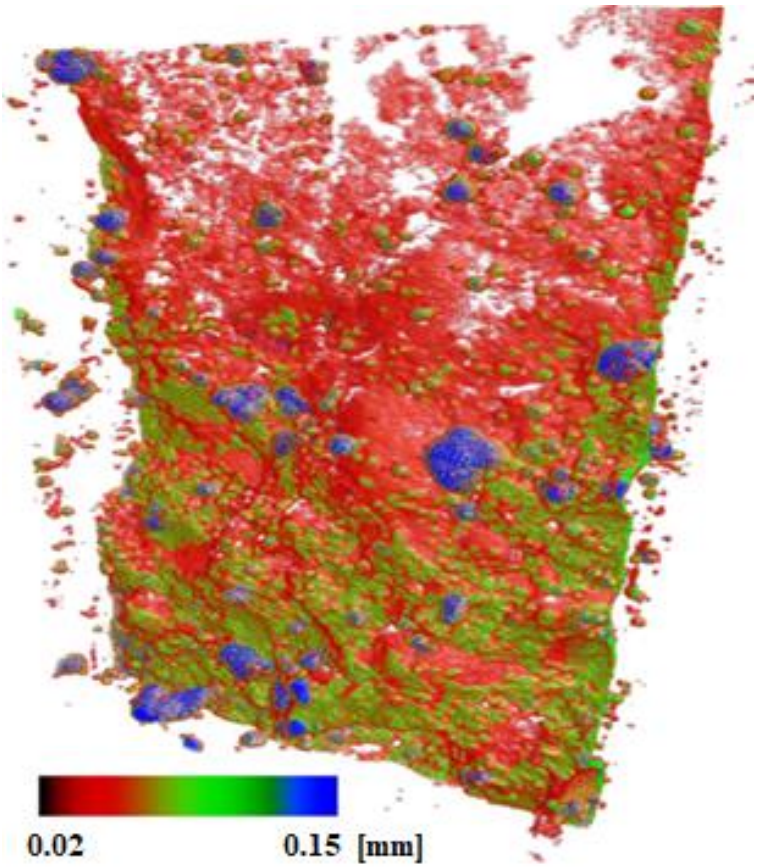

Fig.12: Experimental macro-crack [65] (scale denotes width)

FIGURE 12

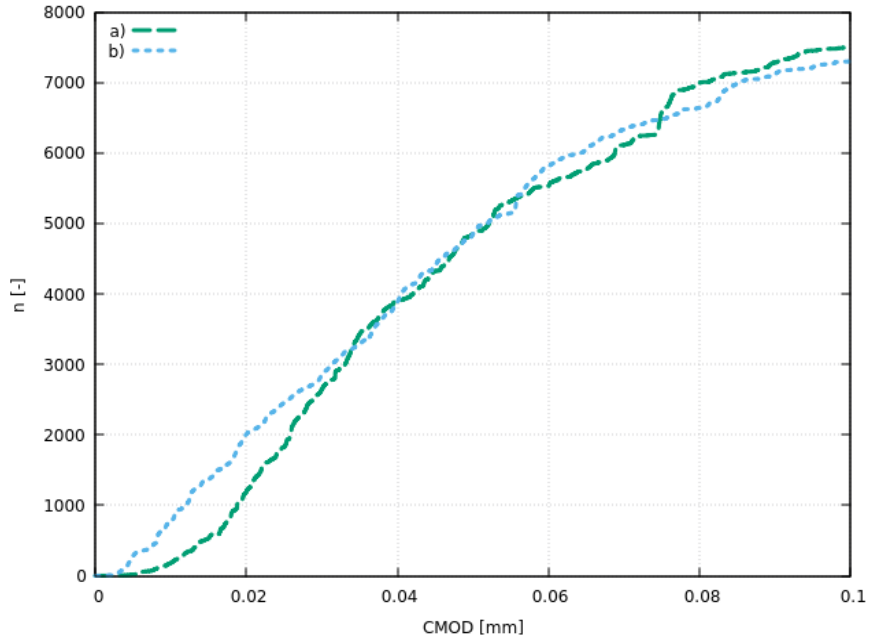

A)

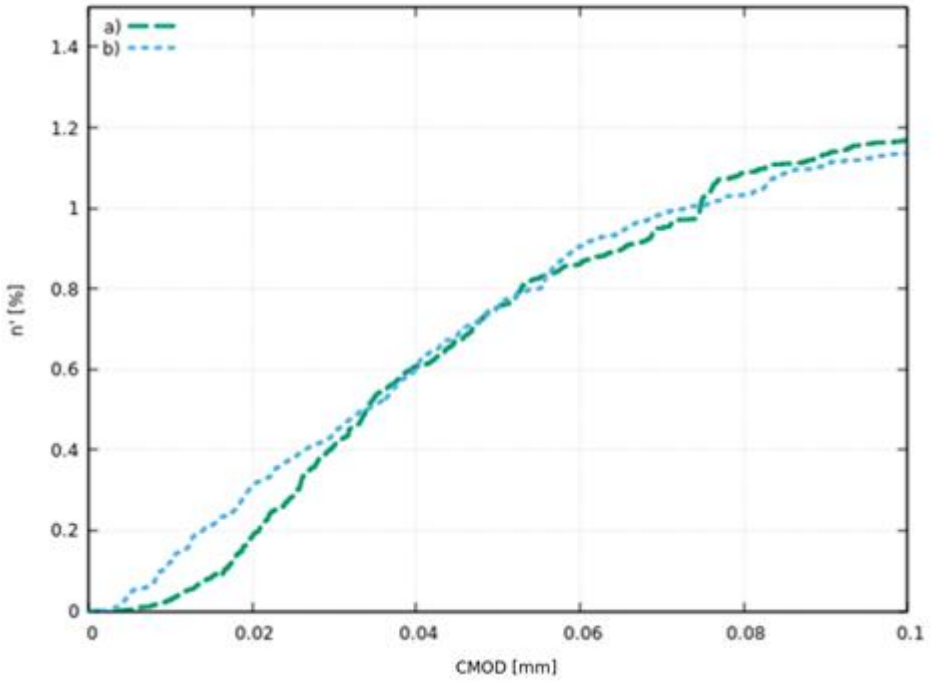

B)

Fig.13: Number of broken contacts *n* (A) and percent content of broken contacts related to initial number of contacts *n*' [%] (B) versus CMOD displacement from 3D DEM simulations with: a) real irregularly-shaped aggregate [10] and b) randomly distributed spherical aggregate

FIGURE 13

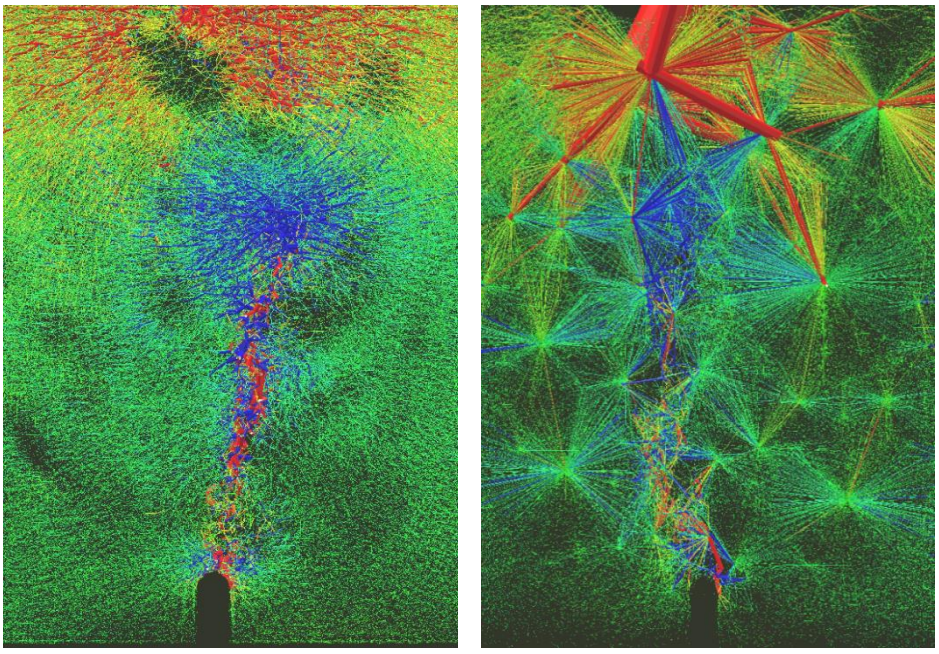

A)

a) b)

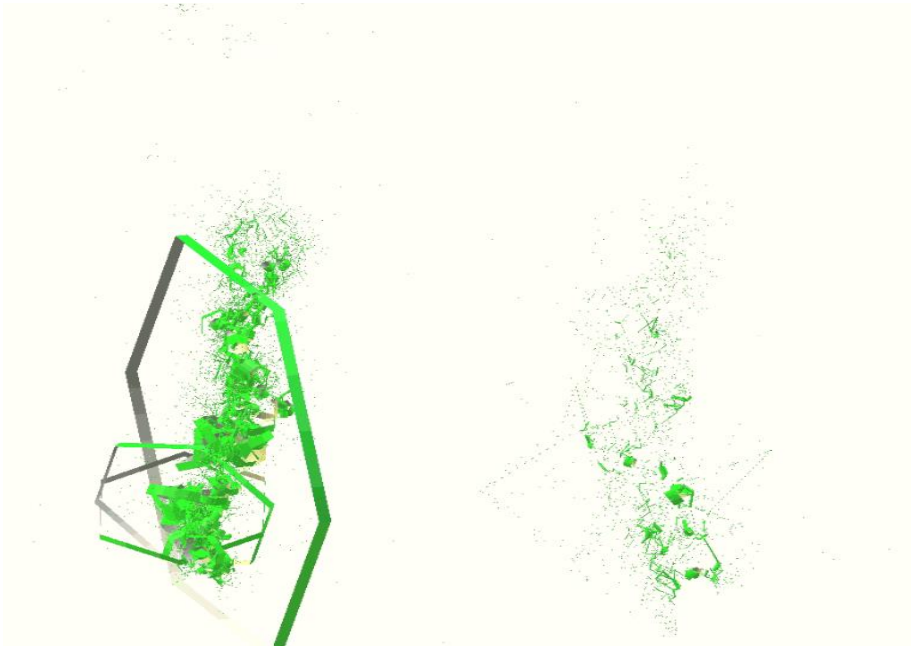

B)

a) b)

Fig.14: Map of (A) normal and (B) tangential contact forces between particles from 3D DEM simulations for CMOD=0.10 mm with: a) real irregularly-shaped aggregate and b) randomly distributed spherical aggregate (red colour denotes large compressive normal forces and blue colour denotes large tensile contact forces, line thickness corresponds to force value)

FIGURE 14

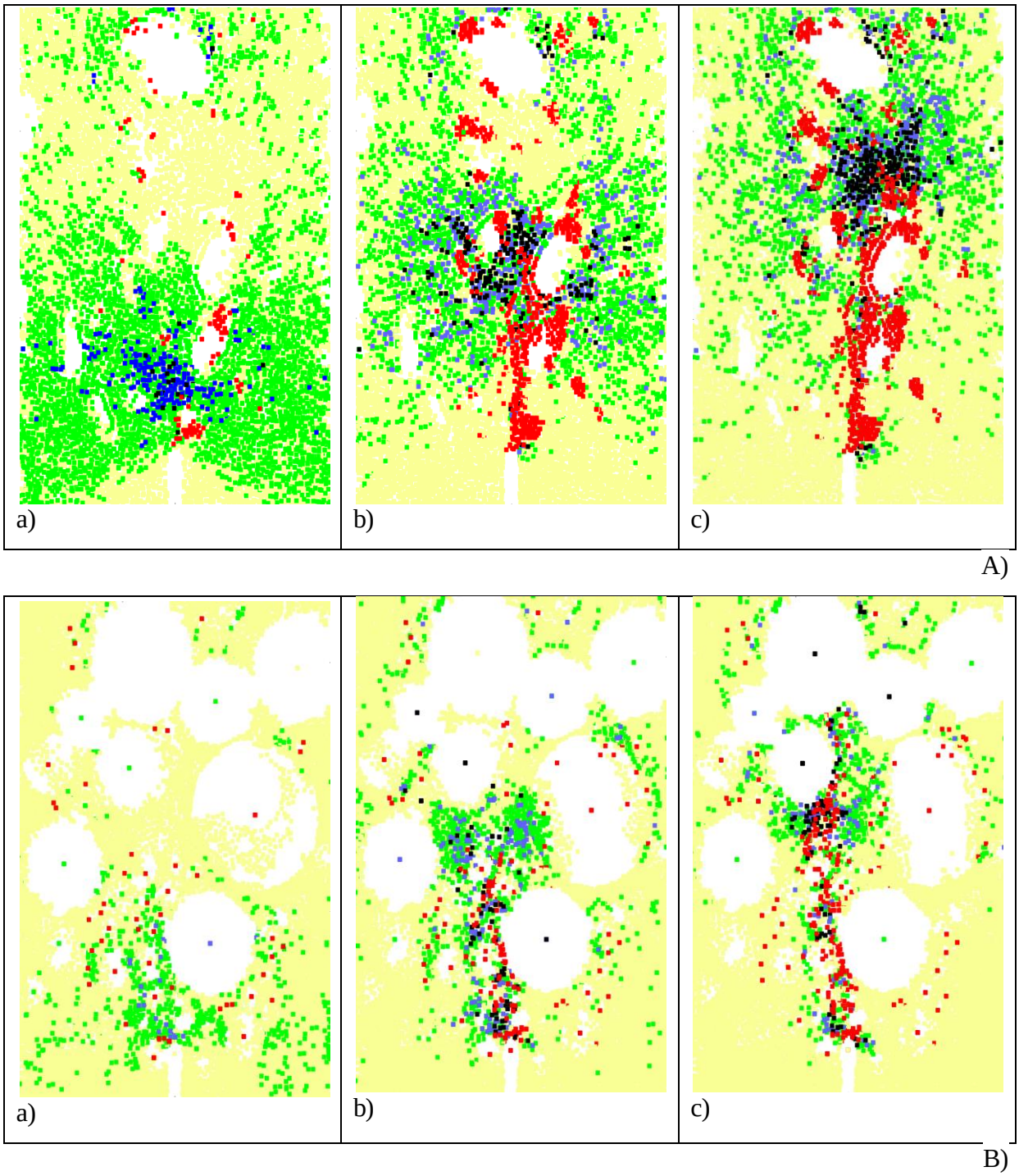

Fig.15: Intensity of tensile normal contact forces in 3D DEM versus CMOD for vertical cross-sectional slice at 3 mm from front specimen side for: A) real irregularly-shaped aggregates [10] and B) randomly distributed spherical aggregates: a) CMOD=0.018 mm, b) CMOD=0.04 mm and c) CMOD=0.10 mm (yellow colour – all contacts, green colour - strained contact forces in 50%, blue colour - strained contact forces in 75%, black colour - strained contact forces in 90% and red colour – broken contacts)

FIGURE 15